catalysts

MDPI

Article

Photocatalytic Degradation of 1,4-Dioxane by Heterostructured Bi_2O_3/Cu-MOF Composites

Wen-Min Wang [1], Lu Zhang [2], Wen-Long Wang [1], Jin-Yi Huang [3], Qian-Yuan Wu [1,*] and Jerry J. Wu [3,*]

[1] State Environmental Protection Key Laboratory of Microorganism Application and Risk Control (SMARC), Guangdong Provincial Engineering Research Center for Urban Water Recycling and Environmental Safety, Institute of Environment and Ecology, Tsinghua Shenzhen International Graduate School, Tsinghua University, Shenzhen 518055, China; wangwm21@mails.tsinghua.edu.cn (W.-M.W.); wwl20@sz.tsinghua.edu.cn (W.-L.W.)

[2] Key Laboratory of Groundwater Resources and Environment, Ministry of Education, Jilin University, Changchun 130026, China; lzhang22@mails.jlu.edu.cn

[3] Department of Environmental Engineering and Science, Feng Chia University, Taichung 407, Taiwan; aa7483569@gmail.com

* Correspondence: wu.qianyuan@sz.tsinghua.edu.cn (Q.-Y.W.); jjwu@mail.fcu.edu.tw (J.J.W.); Tel.: +86-0755-2603-6701 (Q.-Y.W.); +886-4-24517250 (ext. 5206) (J.J.W.)

Abstract: Photocatalysts exhibiting high activity for the degradation of 1,4-dioxane (1,4-D) have been a subject of intense focus due to their high toxicity and challenging degradability. Bismuth oxide (Bi_2O_3) is recognized as an ideal photocatalyst; however, there have been limited studies on its effectiveness in 1,4-D degradation. It is crucial to address the issue of low photocatalytic efficiency attributed to the instability and easy recombination of photogenerated electrons and holes in Bi_2O_3 upon photoexcitation. In this study, Cu-MOF and oxygen vacancy were utilized to improve the 1,4-D photocatalytic degradation efficiency of Bi_2O_3 by preparing Bi_2O_3, Bi_2O_3/Cu-MOF, Bi_2O_{3-x}, and Bi_2O_{3-x}/Cu-MOF. The results revealed that the incorporation of Cu-MOF induced a larger specific surface area, a well-developed pore structure, and a smaller particle size in Bi_2O_3, facilitating enhanced visible light utilization and an improved photoelectron transfer rate, leading to the highest photocatalytic activity observed in Bi_2O_3/Cu-MOF. In addition, oxygen vacancies were found to negatively affect the photocatalytic activity of Bi_2O_3, mainly due to the transformation of the β-Bi_2O_3 crystalline phase into α-Bi_2O_3 caused by oxygen vacancies. Further, the synergistic effect of MOF and oxygen vacancies did not positively affect the photocatalytic activity of Bi_2O_3. Therefore, the construction of heterojunctions using Cu-MOF can significantly enhance the efficiency of degradation of 1,4-D, and Bi_2O_3/Cu-MOF appears to be a promising photocatalyst for 1,4-D degradation. This study opens new avenues for the design and optimization of advanced photocatalytic materials with improved efficiency for the treatment of recalcitrant organic pollutants.

Keywords: bismuth oxide; Cu-MOF; oxygen vacancy; photocatalysis

check for updates

Citation: Wang, W.-M.; Zhang, L.; Wang, W.-L.; Huang, J.-Y.; Wu, Q.-Y.; Wu, J.J. Photocatalytic Degradation of 1,4-Dioxane by Heterostructured Bi_2O_3/Cu-MOF Composites. *Catalysts* **2023**, *13*, 1211. https://doi.org/10.3390/catal13081211

Academic Editor: Rubén Mas Ballesté

Received: 19 July 2023
Revised: 6 August 2023
Accepted: 12 August 2023
Published: 15 August 2023

1. Introduction

1,4-dioxane (1,4-D) has found widespread use in various industrial applications, such as textiles, dyes, pharmaceuticals, pesticides, varnishes, degreasers, and cosmetics, as an industrial solvent stabilizer. Due to its high solubility and low volatility, 1,4-D exhibits remarkable stability, making it a significant threat once released into water bodies and soil through industrial wastewater discharge. More importantly, it poses a considerable risk to human health, as research has indicated a link between 1,4-D exposure and an increased likelihood of cancer, including breast cancer and endometrial cancer [1]. In addition, it negatively impacts certain human sex hormones. 1,4-D has been recognized as a Class 2B carcinogen by the US Environmental Protection Agency [2]. Efforts to mitigate its presence have encountered challenges, with current studies highlighting the inefficiency of biological treatment due to 1,4-D's resistance to biodegradation. Traditional physical methods (e.g., air stripping, carbon adsorption) may also prove inadequate in removing 1,4-D. Although the most effective distillation method exists, it is not widely adopted because of its high cost [3]. Advanced oxidation processes (AOPs) have been considered a promising alternative for 1,4-D degradation, exhibiting significant efficiency [4]. Among these, solar-driven photocatalytic techniques have garnered increasing attention as they offer lower process costs and avoid the utilization of oxidants [5]. However, for the successful degradation of 1,4-D, the development of photocatalysts with high catalytic activity remains essential.

Conventional photocatalysts, such as TiO_2, suffer from poor solar utilization efficiency due to their broad band gap [6,7]. In contrast, Bi_2O_3 offers several advantages, including controllable morphologies (α-Bi_2O_3, β-Bi_2O_3, and γ-Bi_2O_3), a narrow band gap ($\sim$2.80 eV), and good electrical and thermal conductivity, making it an ideal photocatalytic material [8,9]. Nevertheless, the degradation efficiency of 1,4-D by Bi_2O_3 under solar light remains unclear. Additionally, the unstable structure of Bi_2O_3 compounds and the ease of recombination of photogenerated electrons and holes contribute to its low photocatalytic efficiency. Various modification methods have been attempted to improve the photocatalytic activity of Bi_2O_3. One effective approach for Bi_2O_3 modification involves constructing heterostructures, leading to the development of novel photocatalytic materials, such as Bi_2O_3/TiO_2 [10], Bi_2O_3/g-C_3N_4 [11], $Bi_2O_3/Bi_2O_2CO_3$ [12], and $Bi_2O_3/Bi_2S_3/MoS_2$ [13]. These heterostructures effectively modulate the energy band structure and facilitate electron transfer at the interface. At the same time, they increase the specific surface area of the material and expose more active sites, thereby improving the overall photocatalytic activity [14].

Metal organic frameworks (MOFs) are polycrystalline coordination polymers with a multidimensional stereospecific structure, formed by combining metal ions (or metal oxide clusters) with organic ligand molecules through coordination bonds. They have the advantages of high specific surface area, structural stability, and adjustable pore size, making them highly attractive for applications in photocatalysis, gas separation, and storage [15]. The use of MOF materials in constructing heterogeneous structures can significantly enhance the photocatalytic activity of catalysts. For example, Akbarzadeh et al. [16] developed the Cu-MOF/rGO/Ag_3VO_4 for photocatalytic degradation of AB92 dye with a 3-h degradation efficiency of 93.75%. Moreover, vacancy engineering, especially focusing on oxygen vacancies, has made great progress in the field of photocatalysis. In general, oxygen vacancies in photocatalysts can effectively improve light absorption and promote charge separation efficiency by creating unsaturated sites on the surface [17]. Ding et al. [18] successfully prepared HS-$CuFe_2O_4$-σ with abundant oxygen vacancies, leading to a remarkable 20-fold increase in the rate of ciprofloxacin degradation at neutral pH. Similarly, Zou et al. [19] designed MOF-derived Bi_2O_3@C with abundant oxygen vacancies, demonstrating highly efficient photodegradation of tetracycline hydrochloride with an 88% removal rate within just 120 min. These findings suggest that the utilization of MOFs in constructing heterostructures or inducing oxygen vacancies may hold great potential in enhancing the photocatalytic degradation of 1,4-D. However, few studies have been conducted on the individual and synergistic effects of MOF-constructed heterostructures and oxygen vacancies on the 1,4-D degradation by Bi_2O_3. Therefore, exploring these aspects could prove to be significant for advancing the field of photocatalysis.

This study aimed to address the research gap concerning the photocatalytic degradation of 1,4-D by Bi_2O_3. To achieve this, the individual contributions of MOF-constructed heterojunctions and oxygen vacancy engineering to enhancing the photocatalytic activity of Bi_2O_3 in the degradation of 1,4-D were investigated. Furthermore, the study explored the synergistic effects resulting from the combination of MOF-constructed heterojunctions and oxygen vacancies, providing valuable insights into the overall catalytic mechanism. For this purpose, Bi_2O_3-related photocatalysts were prepared using a simple microwave method to degrade 1,4-D. Four photocatalysts, namely, Bi_2O_3, Bi_2O_3/Cu-MOF, Bi_2O_{3-x}, and Bi_2O_{3-x}/Cu-MOF, were synthesized to explore the effects of MOF-constructed heterostructures and oxygen vacancies on the photocatalytic activity. The factors and mechanism that enhance the photocatalytic activity of Bi_2O_3 were elucidated by analyzing the characterization results and optical properties of these as-prepared photocatalysts. In addition, degradation experiments were conducted to determine the 1,4-D degradation efficiency of the above-mentioned Bi_2O_3-based photocatalysts.

2. Results and Discussion

2.1. Characterizations

2.1.1. Morphology and Structure

The morphology and microstructure of the samples were observed through FE-SEM and TEM analysis. Cu-MOF displayed an octahedral structure, typical of HKUST-1 MOF crystals, confirming the successful synthesis of Cu-MOF, as shown in Figure 1 [20]. Bi_2O_3 presented a sphere-like structure with an average diameter of about 1–2 μm (Figure 2a). Further examination at high magnification revealed that the peripheries of microsphere formations were constructed from abundant ultrathin nanosheets, each measuring approximately 10 nm in thickness. Bi_2O_3/Cu-MOF microsphere showed a more advanced porous structure compared to Bi_2O_3 (Figure 2b). This porous structure was conducive to increasing the active sites and promoting interfacial charge transfer, which was beneficial for the photodegradation [21]. With the introduction of oxygen vacancy, the Bi_2O_{3-x} microsphere agglomerated (Figure 2c). The nanosheets on the surface of Bi_2O_{3-x} microspheres collapsed and sporadically attached irregular particles, potentially obstructing the active sites. Bi_2O_{3-x}/Cu-MOF exhibited an irregular shape, and the nanosheets on its surface disappeared (Figure 2d). The low-magnification TEM images corroborated the SEM results. It is noteworthy that the TEM image of Bi_2O_3/Cu-MOF also showcased the presence of more advanced pore structures.

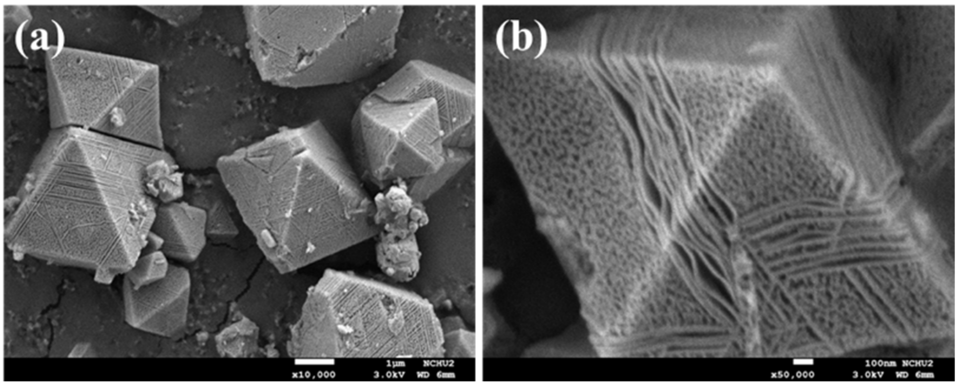

Figure 1. FE-SEM images of Cu-MOF with different magnitudes of (**a**) ×10,000 and (**b**) ×50,000.

2.1.2. XRD Analysis

XRD analysis was performed to characterize the crystallinity and crystal phase of Cu-MOF, Bi_2O_3, Bi_2O_3/Cu-MOF, Bi_2O_{3-x}, and Bi_2O_{3-x}/Cu-MOF photocatalysts, as shown in Figure 3. The XRD pattern of Cu-MOF matched well with the simulated pattern of $Cu_3(BTC)_2 \cdot 3H_2O$ (also known as HKUST-1) [22]. The main peaks of Cu-MOF were located at 6.7°, 9.46°, 11.62°, 13.42°, 14.62°, 16.42°, 17.44°, 19.02°, 20.1°, 21.24°, 23.38°, 24.06°, 25.94°, 28.66°, and 29.32°, which correspond to the (200), (220), (222), (400), (331), (422), (511), (440), (600), (620), (444), (551), (731), (733), and (751) planes, respectively (JCPDS card No. 00-062-1183) [23,24].

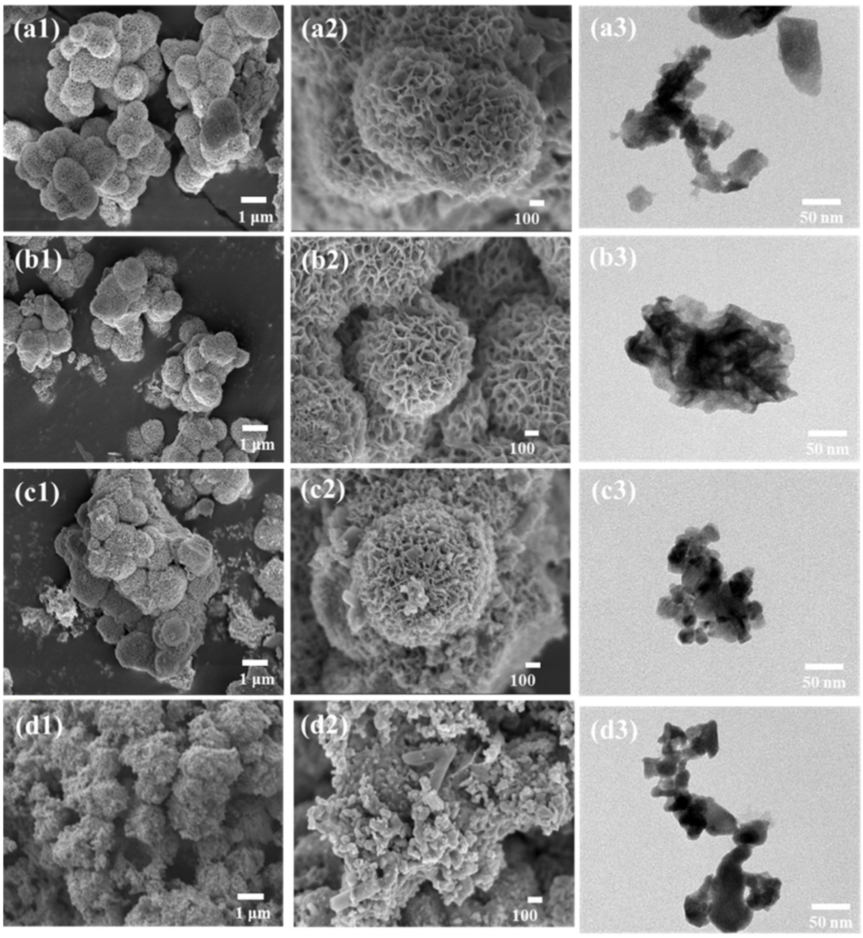

Figure 2. FE-SEM ((**a1**,**a2**,**b1**,**b2**,**c1**,**c2**,**d1**,**d2**) with different magnitudes) and TEM images (**a3**,**b3**,**c3**,**d3**) of (**a**) Bi_2O_3, (**b**) Bi_2O_3/Cu-MOF, (**c**) Bi_2O_{3-x}, (**d**) Bi_2O_{3-x}/Cu-MOF.

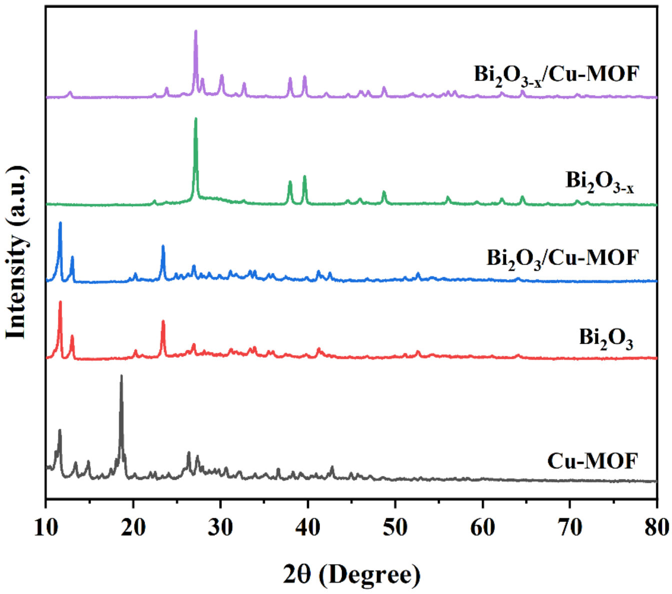

Figure 3. XRD patterns of Cu-MOF, Bi_2O_3, Bi_2O_3/Cu-MOF, Bi_2O_{3-x}, and Bi_2O_{3-x}/Cu-MOF.

There were no significant changes in the characteristic peaks of Bi_2O_3 and Bi_2O_{3-x} after Cu-MOF doping, indicating that the addition of Cu-MOF had negligible effects on the crystalline structure of the Bi_2O_3/Cu-MOF and Bi_2O_{3-x}/Cu-MOF composite photocatalysts [25]. The main diffraction peaks of Bi_2O_3 and Bi_2O_3/Cu-MOF were located at 2θ values of 10.07°, 23.22°, and 26.38°, which could be well indexed to the (004), (101), and (105) planes, respectively, of β-Bi_2O_3 (JCPDS 76-2477) [26]. Both Bi_2O_3 and Bi_2O_3/Cu-MOF exhibited metastable phase β-Bi_2O_3 due to the microwave synthesis method, which promoted the formation of metastable phases by controlling the reaction kinetics [27]. The main diffraction peaks of Bi_2O_{3-x} and Bi_2O_{3-x}/Cu-MOF were located at 2θ values of 26.92°, 37.60°, 40.05°, and 48.58°, which could be well indexed to the (111), (112), (−222), and (−104) planes, respectively, of α-Bi_2O_3 (PDF NO. 41-1449) [28]. The generation of oxygen vacancies transformed metastable phase β-Bi_2O_3 into the stable α-Bi_2O_3, indicating that oxygen vacancy significantly influenced the crystal structure of the catalyst.

2.1.3. XPS Analysis

X-ray photoelectron spectroscopy (XPS) was employed to determine the chemical compositions and surface chemical states of Bi_2O_3, Bi_2O_3/Cu-MOF, Bi_2O_{3-x}, and Bi_2O_{3-x}/Cu-MOF, as shown in Figure 4. The surface composition elements of the four photocatalysts were detected as Bi and O (Figure 4a).

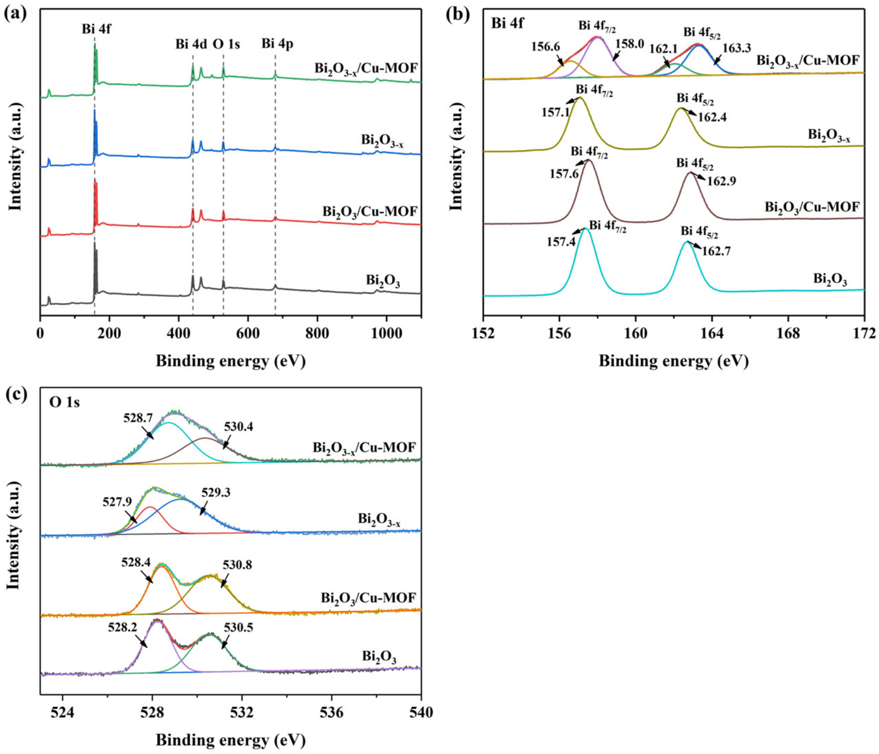

Figure 4. XPS spectra of (**a**) a wide survey, (**b**) Bi 4f, and (**c**) O 1s over Bi_2O_3, Bi_2O_3/Cu-MOF, Bi_2O_{3-x}, and Bi_2O_{3-x}/Cu-MOF.

Figure 4b shows the high-resolution XPS spectra of Bi element. The Bi_2O_3 spectrum exhibited two characteristic peaks located at 157.4 eV and 162.7 eV, which should be assigned to Bi $4f_{5/2}$ and Bi $4f_{7/2}$ regions of Bi^{3+} species, respectively [29]. When Cu-MOF was introduced, the characteristic peaks of Bi shifted to higher binding energies (157.6 eV and 162.9 eV), suggesting that the Cu-MOF introduction induced the electron transfer of Bi to the surrounding adjacent atoms, leading to a more positive valence state than Bi^{3+} species of the Bi element in Bi_2O_3/Cu-MOF. In contrast, the characteristic peaks of Bi in Bi_2O_{3-x} shifted to lower binding energies (157.1 eV and 162.4 eV), which should be ascribed to the presence of oxygen vacancies [19]. Furthermore, the peaks of Bi $4f_{5/2}$ and Bi $4f_{7/2}$ of Bi_2O_{3-x}/Cu-MOF could be subdivided into two peaks, respectively, probably due to the combined effect of MOF and oxygen vacancies. It can be deduced that most of the Bi element was affected by the Cu-MOF, with peaks shifting towards higher binding energies

(158.0 eV and 163.3 eV), while a small proportion shifted to lower binding energies due to the presence of oxygen vacancies (156.6 eV and 162.1 eV).

Figure 4c shows the high-resolution XPS spectra of the O element. In the spectrum of Bi_2O_3, the peaks at 528.2 eV and 530.5 eV should be attributed to the Bi−O bond and adsorbed oxygen, respectively [30]. The corresponding peaks of the O element in Bi_2O_3/Cu-MOF shifted to higher binding energies (528.4 eV and 530.8 eV). This shift could be attributed to the rebalancing of inner electrons, proving a strong interfacial interaction between the Bi_2O_3 and Cu-MOF heterojunction, which was beneficial for the separation and transfer of the photogenerated charge carrier [31]. Bi_2O_{3-x} appeared as two peaks located at 527.9 eV and 529.3 eV, which should be attributed to the Bi−O bond and oxygen vacancy [32]. These two peaks also shifted towards higher binding energies in Bi_2O_{3-x}/Cu-MOF, consistent with the shift of O 1s in Bi_2O_3/Cu-MOF. Therefore, the introduction of Cu-MOF usually resulted in a positive shift of the O1s peak. Moreover, it was noteworthy that the peak intensity of the oxygen vacancy in Bi_2O_{3-x}/Cu-MOF was much lower than that in Bi_2O_{3-x}. This phenomenon indicated that the introduction of Cu-MOF led to the generation of even fewer oxygen vacancies.

2.1.4. BET and Particle Size Analysis

The BET-specific surface area (S_{BET}) of photocatalysts was determined through the N_2 adsorption–desorption experiment, and the results are shown in Table 1. Upon the introduction of Cu-MOF, the specific surface area of Bi_2O_3 increased from 5.09 m^2/g (Bi_2O_3) to 9.52 m^2/g (Bi_2O_3/Cu-MOF), and that of Bi_2O_{3-x} increased from 6.08 m^2/g (Bi_2O_{3-x}) to 7.81 m^2/g (Bi_2O_{3-x}/Cu-MOF). The favorable increase in the specific surface area might be due to its framework structure, which is consistent with previous findings [19]. At the same time, the presence of oxygen vacancies also contributed to the increase in the specific surface area. The expanded surface area allowed for more active sites, facilitating easy transport of charge carriers, and ultimately enhancing the photocatalytic activity [17,33]. Notably, Bi_2O_3/Cu-MOF exhibited the highest S_{BET} value (9.52 m^2/g) among the prepared photocatalysts, in agreement with the porous structure observed by SEM.

Table 1. S_{BET} of Bi_2O_3, Bi_2O_3/Cu-MOF, Bi_2O_{3-x}, and Bi_2O_{3-x}/Cu-MOF.

Photocatalyst	**Bi_2O_3**	**Bi_2O_3/Cu-MOF**	**Bi_2O_{3-x}**	**Bi_2O_{3-x}/Cu-MOF**
S_{BET} (m^2/g)	5.09	9.52	6.08	7.81

The particle size distribution of the photocatalysts was measured using a laser particle size analyzer, as shown in Figure 5. The median particle diameter (D_{50}) of Bi_2O_3/Cu-MOF (3.89 μm) was smaller than that of Bi_2O_3 (4.39 μm) and the D_{50} of Bi_2O_{3-x}/Cu-MOF (2.63 μm) was smaller than that of Bi_2O_{3-x} (4.32 μm). These data indicated that the introduction of Cu-MOF was beneficial in reducing the particle size, which could promote photocatalytic activity [34]. Moreover, the D_{50} of Bi_2O_{3-x} was smaller than that of Bi_2O_3 and the D_{50} of Bi_2O_{3-x}/Cu-MOF was smaller than that of Bi_2O_3/Cu-MOF. This result could be attributed to the oxygen vacancy promoting the conversion of crystal from β-Bi_2O_3 to α-Bi_2O_3 with a smaller particle size.

2.1.5. UV-Vis DRS Analysis

The UV-Vis DRS of photocatalysts is shown in Figure 6a. All photocatalysts exhibited strong absorption in the UV region (220–300 nm). Specifically, Bi_2O_3 displayed the highest absorption intensity in the UV region (220–350 nm) but the weakest absorption intensity in the visible region (400–800 nm). Upon the introduction of Cu-MOF, the absorption intensity of Bi_2O_3/Cu-MOF and Bi_2O_{3-x}/Cu-MOF decreased in the UV region, while it increased in the visible region. This change could be attributed to the unique d–d transition of the Cu ions in Cu-MOF and the strong interaction between Bi_2O_3 or Bi_2O_{3-x}

and Cu-MOF [35,36]. The enhanced light absorption in the visible region could provide more photogenerated charge carriers, leading to enhanced photocatalytic activity [37]. In addition, it was observed that the absorption intensity of Bi_2O_{3-x} was higher than that of Bi_2O_3, and Bi_2O_{3-x}/Cu-MOF exhibited higher absorption intensity than Bi_2O_3/Cu-MOF in the visible region. This phenomenon elucidated that the presence of oxygen vacancies could enhance the absorption intensity within the visible spectral range. The absorption peaks of Cu-MOF, Bi_2O_3/Cu-MOF, and Bi_2O_{3-x}/Cu-MOF at approximately 700 nm might be caused by the spin-enabled transition of the material [33]. Therefore, the introduction of Cu-MOF and oxygen vacancies had the potential to enhance the utilization efficiency of visible light.

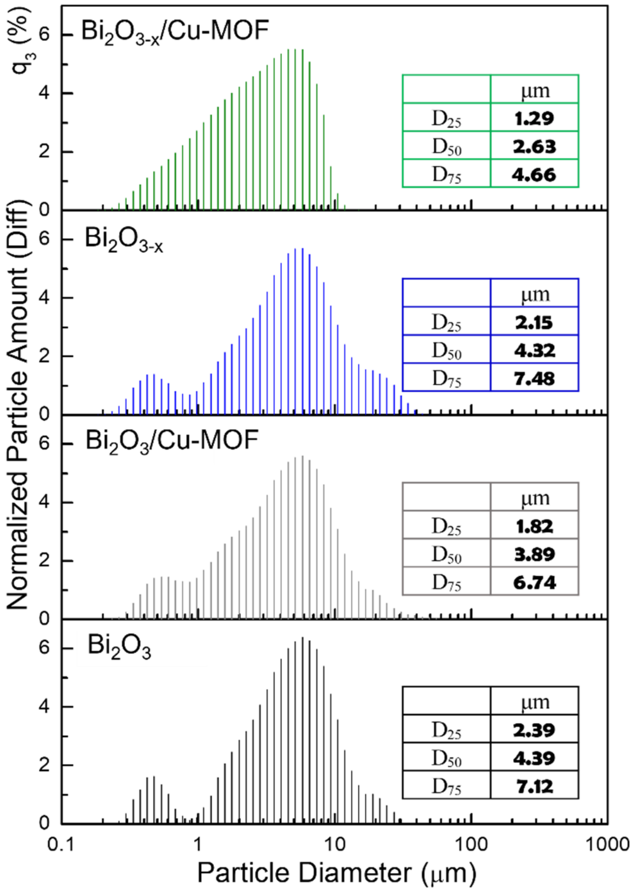

Figure 5. Particle size distribution of Bi_2O_3, Bi_2O_3/Cu-MOF, Bi_2O_{3-x}, and Bi_2O_{3-x}/Cu-MOF.

Based on UV-Vis DRS spectra and Tauc's approach (Equation (1)) [38], the bandgap (E_g) values of photocatalysts were calculated and are presented in Figure 6b and Table 2. Obviously, the band gap of Bi_2O_3/Cu-MOF (3.30 eV) was smaller than that of Bi_2O_3 (3.54 eV), and that of Bi_2O_{3-x}/Cu-MOF (2.19 eV) was smaller than that of Bi_2O_{3-x} (3.30 eV). The reduction in the band gaps of Bi_2O_3/Cu-MOF and Bi_2O_{3-x}/Cu-MOF was mainly attributed to the heterojunction formed between Bi_2O_3 or Bi_2O_{3-x} and Cu-MOF [17]. The narrow band gap allows electrons to be excited from the valence band (VB) to the conduction band (CB) with less energy, which facilitates the separation and transfer of photogenerated electrons and holes and improves photocatalytic activity [34,39]. Moreover, the band gap of Bi_2O_{3-x} (3.30 eV) was smaller than that of Bi_2O_3 (3.54 eV), and the band gap of Bi_2O_{3-x}/Cu-MOF (2.19 eV) was smaller than that of Bi_2O_3/Cu-MOF (3.30 eV). These results demonstrated that oxygen vacancies could effectively reduce the band gap, consistent with the findings of Zhao et al. [17].

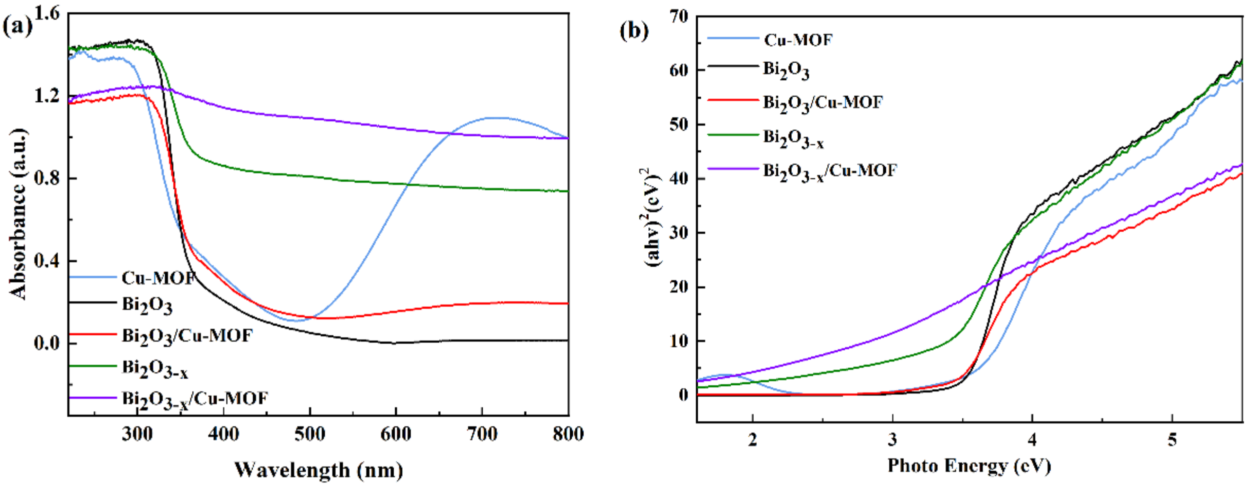

Figure 6. (**a**) UV-Vis absorption spectra and (**b**) Tauc's plots of Cu-MOF, Bi_2O_3, Bi_2O_3/Cu-MOF, Bi_2O_{3-x}, and Bi_2O_{3-x}/Cu-MOF.

$$[(\alpha h\upsilon)^{1/n} = A(h\upsilon - E_g)] \tag{1}$$

where α is the absorption coefficient, hv is the photo energy, A is a constant, and n is either 1/2 for a direct transition or 2 for an indirect transition.

Table 2. Band gap energies of Cu-MOF, Bi_2O_3, Bi_2O_3/Cu-MOF, Bi_2O_{3-x}, and Bi_2O_{3-x}/Cu-MOF.

Photocatalyst	Band Gap (eV)
Cu-MOF	3.59
Bi_2O_3	3.54
Bi_2O_3/Cu-MOF	3.46
Bi_2O_{3-x}	3.30
Bi_2O_{3-x}/Cu-MOF	2.19

2.1.6. PL Spectra Analysis

Fluorescence emission detection (PL) was employed to determine the charge generation rate and the recombination of photo-generated electrons and holes. A low fluorescence intensity suggested a low recombination rate and a high electron transfer efficiency, leading to an improvement in the photocatalytic activity. The PL spectra of Bi_2O_3, Bi_2O_3/Cu-MOF, Bi_2O_{3-x}, Bi_2O_{3-x}/Cu-MOF, and Cu-MOF are shown in Figure 7. Cu-MOF showed a low-level peak intensity within the wavelength range of 400~800 nm, indicating its low recombination rate and higher electron transfer efficiency. Distinctive peaks were observed around 649.8 nm and 818.7 nm in Bi_2O_3, Bi_2O_3/Cu-MOF, Bi_2O_{3-x}, and Bi_2O_{3-x}/Cu-MOF, with the peak intensity following the order of Bi_2O_3 > Bi_2O_3/Cu-MOF > Bi_2O_{3-x} > Bi_2O_{3-x}/Cu-MOF. This trend suggested that the introduction of Cu-MOF reduced the recombination of electrons and holes due to the lower peak intensity observed in Bi_2O_3/Cu-MOF compared to Bi_2O_3 and in Bi_2O_{3-x}/Cu-MOF compared to Bi_2O_{3-x}. This effect was attributed to the presence of heterojunctions. Furthermore, the peak intensity of Bi_2O_{3-x} was lower than that of Bi_2O_3, and the peak of Bi_2O_{3-x}/Cu-MOF was lower than that of Bi_2O_3/Cu-MOF, suggesting that the presence of oxygen vacancies significantly enhanced the separation efficiency of photoinduced carriers and reduced the recombination of electrons and holes. Therefore, both heterojunctions and oxygen vacancies proved to be effective in reducing the recombination efficiency of electron holes.

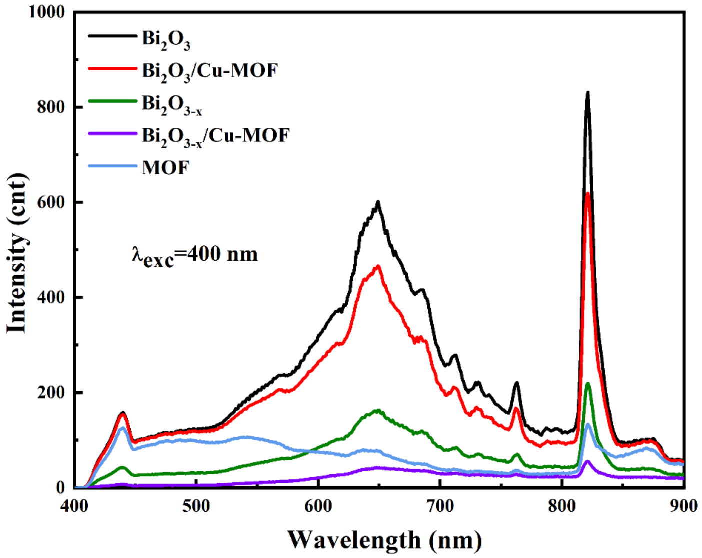

Figure 7. PL spectra of as-synthesized Cu-MOF, Bi_2O_3, Bi_2O_3/Cu-MOF, Bi_2O_{3-x}, and Bi_2O_{3-x}/Cu-MOF photocatalysts.

2.2. Photocatalytic Activity Performance

To evaluate the effect of heterojunction construction and oxygen vacancy on the performance of the photocatalyst, experiments were conducted for photocatalytic degradation of 1,4-D using the prepared catalysts. Figure 8a shows that the removal efficiency of 1,4-D during the dark adsorption–desorption phase was negligible, indicating minimal adsorption of 1,4-D onto the surfaces of the photocatalysts. During the photocatalytic stage, the 1,4-D removal efficiency followed the order of Bi_2O_3/Cu-MOF (68.7%) > Bi_2O_3 (62.8%) > Bi_2O_{3-x}/Cu-MOF (52.2%) > Bi_2O_{3-x} (47.1%) within 180 min, with the kinetic rate constant (k_{obs}) values following the same order (Figure 8b). Table 3 shows the 1,4-D removal efficiency of different photocatalysts. It was found that Bi_2O_3/Cu-MOF exhibited higher photocatalytic activity for 1,4-D degradation compared to most of those previously reported. The enhanced photocatalytic activity of Bi_2O_3/Cu-MOF could be attributed to several factors: (i) the advanced porous structure, large specific surface area, and small particle size providing a large number of active sites; (ii) the heterojunction promoting visible light utilization, electron transfer rate, and efficient separation of photogenerated electron–hole pairs [40]; and (iii) the catalytic activity of the crystal structure of β-Bi_2O_3 (Bi_2O_3 and Bi_2O_3/Cu-MOF) being higher than that of α-Bi_2O_3 (Bi_2O_{3-x} and Bi_2O_{3-x}/Cu-MOF) [28].

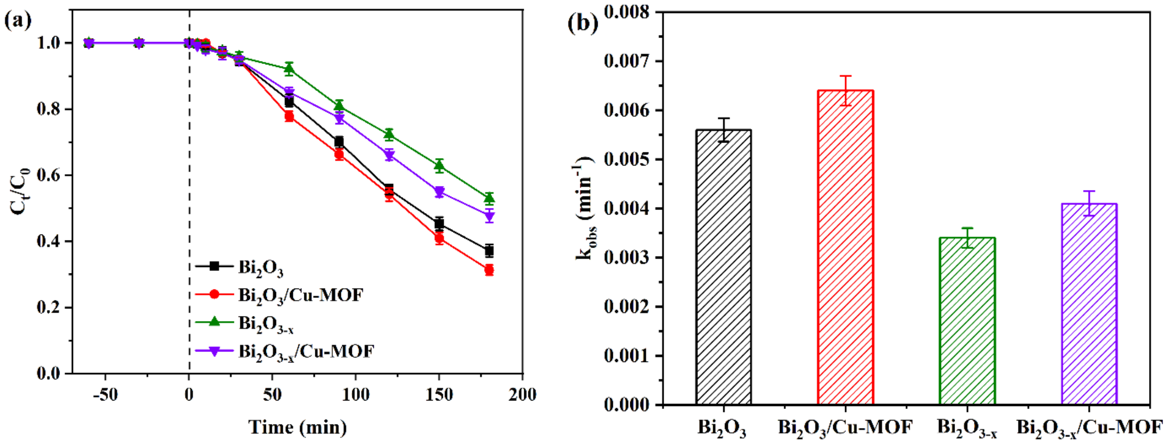

Figure 8. Photocatalytic activities of Bi_2O_3, Bi_2O_3/Cu-MOF, Bi_2O_{3-x}, and Bi_2O_{3-x}/Cu-MOF: (**a**) removal efficiency of 1,4-D and (**b**) reaction rate constant (k_{obs}).

Table 3. Comparison of photocatalytic activities of photocatalysts for 1,4-D removal.

Photocatalyst	Light Source	Catalyst Dosage (g/L)	1,4-D Concentration (mg/L)	Time (min)	1,4-D Removal Efficiency (%)	References
Fe/nAl	Solar	0.3	50	180	about 22	[5]
WO_3/nγ-Al_2O_3	Solar	0.3	50	180	56.67	[41]
TiO_2	Xenon light (2 kW)	0.5	500	180	about 10	[42]
Au–TiO_2	Xenon light (2 kW)	0.5	500	240	59	[43]
Cu-ZnO	Solar	0.3	355	180	43.9	[44]
Bi_2O_3/Cu-MOF	Xenon light (350 W)	0.06	50	180	68.7	This study

Despite Bi_2O_{3-x} and Bi_2O_{3-x}/Cu-MOF with oxygen vacancies exhibiting excellent optical properties, such as strong adsorption in the visible region, a small band gap, and weak PL peak intensity, their photocatalytic activity was inferior compared to that of Bi_2O_3 and Bi_2O_3/Cu-MOF. This difference may be attributed to the following reasons: (i) the crystal structure of β-Bi_2O_3 (Bi_2O_3 and Bi_2O_3/Cu-MOF) having higher catalytic activity than α-Bi_2O_3 (Bi_2O_{3-x} and Bi_2O_{3-x}/Cu-MOF) [28]; (ii) the oxygen vacancy structure leaving two electrons due to the charge compensation effect, occupying the position of photoexcited electrons, which leads to a decrease in the number of oxidative holes (h^+) [18]; and (iii) the introduction of oxygen vacancies lowering the zero charge points of Bi_2O_{3-x} and Bi_2O_{3-x}/Cu-MOF below the solution pH value, thereby inhibiting the degradation of 1,4-D due to its negatively charged-surface [4].

In summary, heterojunctions can significantly improve the structure and optical properties of the materials, while promoting photocatalytic activity. On the other hand, although oxygen vacancies could improve the optical properties of the materials, they are not conducive to the oxidation reaction in the photocatalytic system.

2.3. Photocatalytic Mechanisms

Based on the above discussion, Bi_2O_3/MOF was a composite of β-Bi_2O_3 and $Cu_3(BTC)_2 \bullet 3H_2O$ (Cu-MOF). The values of VB and CB of β-Bi_2O_3 and Cu-MOF were calculated using Equations (1) and (2) [45]. The X values of β-Bi_2O_3 and Cu-MOF were 6.12 eV and 5.72 eV [45,46]. Through calculations, it was determined that the E_{VB} and E_{CB} of β-Bi_2O_3 are 3.39 eV and −0.15 eV, and the E_{VB} and E_{CB} of Cu-MOF are about 3.02 eV and −0.57 eV.

$$E_{VB} = X - E_e + 0.5E_g \tag{2}$$

$$E_{CB} = E_{VB} - E_g \tag{3}$$

where E_g is the band gap of the semiconductor, E_{VB} is the VB edge potential, E_{CB} is the CB edge potential, E_e is the free electron energy (4.5 eV) on the NHE (pH = 7), and X is the electronegativity of the semiconductor.

As reported, β-Bi_2O_3 and Cu-MOF are n-type semiconductors with a Fermi energy level (E_f) close to its CB [9,46], forming an n-n heterojunction between β-Bi_2O_3 and Cu-MOF. Since the E_f of Cu-MOF is located at more negative potential than β-Bi_2O_3, when β-Bi_2O_3 and Cu-MOF form a heterojunction interface, electrons flow from the CB of Cu-MOF to the CB of β-Bi_2O_3 to reach the balanced state of the Fermi level [47]. This phenomenon is evidenced by the peak shift of Bi and the O shift in the XPS results (Figure 4b,c). The electron flow causes the interface region of β-Bi_2O_3 to become negatively charged and Cu-MOF to become positively charged, resulting in the β-Bi_2O_3 surface bending downward and the Cu-MOF surface bending upward [48]. Meanwhile, the space charge layer generated at the interface creates an internal potential gradient to oppose the electron flow, which facilitates the migration of photoinduced charge carriers [49].

The possible photocatalytic mechanism of the Bi_2O_3/MOF photocatalyst for 1,4-D degradation is proposed as shown in Figure 9. When irradiated by visible light, β-Bi_2O_3 and Cu-MOF absorb photons in response to visible light, and thus electrons (e^-) in VB are transferred from VB to CB, resulting in the formation of holes (h^+) in VB (Equations (4) and (5)). On the one hand, e^- are consumed in the CBs under the action of dissolved oxygen (O_2) (Equation (6)) and the acidic environment (Equation (7)), which further inhibits electron–hole recombination. Importantly, oxidizing superoxide anion radicals ($\cdot O_2{}^-$) are generated from O_2 (-0.046 eV for $O_2/\cdot O_2{}^-$). On the other hand, the h^+ have enough potential to oxidize water molecules (2.37 eV for $H_2O/\cdot OH$), leading to the generation of hydroxyl radicals ($\cdot OH$) (Equation (8)) [50]. Therefore, $\cdot O_2{}^-$, $\cdot OH$, and h^+ collectively contribute to the degradation of 1,4-D.

$$Bi_2O_3 + hv \rightarrow e^- + h^+ \tag{4}$$

$$MOF + hv \rightarrow e^- + h^+ \tag{5}$$

$$O_2 + e^- \rightarrow H^+ + \bullet O_2^- \tag{6}$$

$$H^+ + e^- \rightarrow H_2 \tag{7}$$

$$H_2O + h^+ \rightarrow \bullet OH \tag{8}$$

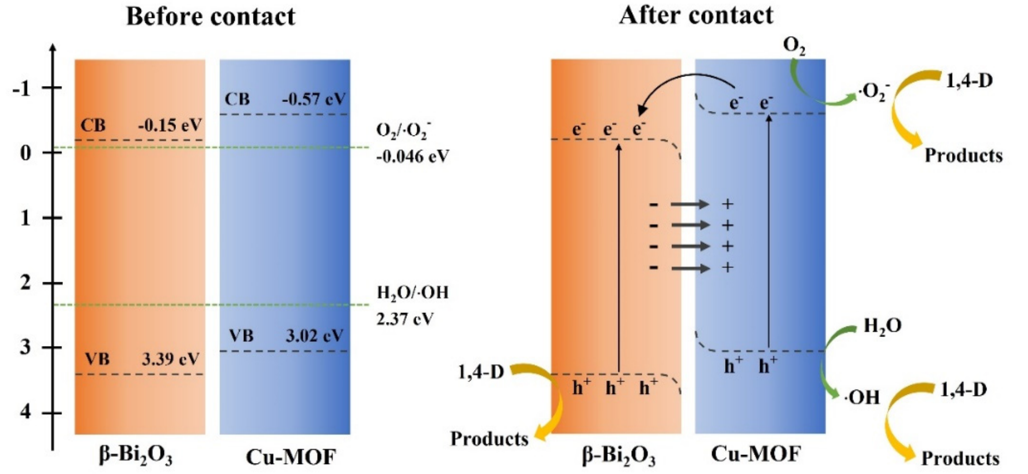

Figure 9. Proposed photocatalytic mechanism for the Bi_2O_3/MOF photocatalyst.

3. Methods

3.1. Materials

All chemicals were of the highest purity and were used directly without further purification. 1,3,5-benzenetricarboxylic acid ($C_9H_6O_6$, H_3BTC), ethylene glycol ($(CH_2OH)_2$, EG), polyethylenglycol ($C_{2n}H_{4n+2}O_{n+1}$, PEG), bismuth (III) nitrate pentahydrate ($Bi(NO_3)_3 \cdot 5H_2O$), copper (II) nitrate trihydrate ($Cu(NO_3)_2 \cdot 3H_2O$), and sodium borohydride ($NaBH_4$) were purchased from SHOWA (Tokyo, Japan). 2-propanol (C_3H_8O, IPA), ethanol (C_2H_5OH, EtOH), dimethyl sulfoxide (C_2H_6OS, DMSO), and Dimethylformamide (C_3H_7NO, DMF), 1, 4-D ($C_4H_8O_2$) were obtained from Acros (Morris Plains, NJ, USA). The 1,4-D stock solution (1000 mg/L) was prepared by dissolving 0.97 mL of 1,4-D in deionized (DI) water to yield a 1 L solution. DI water (Milli-Q Plus, resistance = 18.2 MΩ) was used for all experiments.

3.2. Synthesis of Composite Photocatalysts

The preparation processes of all photocatalysts are shown in Figure 10.

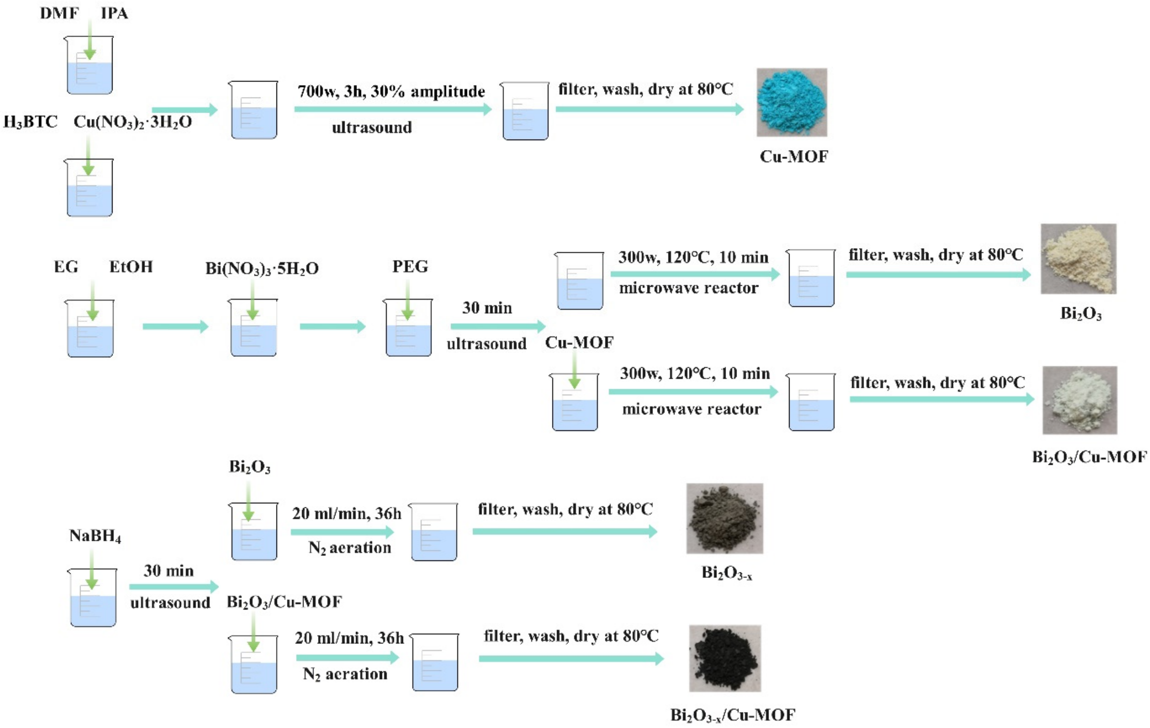

Figure 10. Preparation process of Cu-MOF, Bi_2O_3, Bi_2O_3/Cu-MOF, Bi_2O_{3-x}, and Bi_2O_{3-x}/Cu-MOF.

3.2.1. Cu-MOF

The Cu-MOF was synthesized using the ultrasonic method. Firstly, a 50 mL mixed solution was prepared by adding DMF, IPA, and DI water at a volume ratio of 1:1:1. Subsequently, 0.4200 g of H_3BTC and 1.8301 g of $Cu(NO_3)_2{\cdot}3H_2O$ were dissolved in the mixed solution to obtain solution A and solution B, respectively. Then, solution B was added dropwise into solution A under continuous stirring for 30 min. Next, the resulting mixture was irradiated with high-intensity ultrasound (700 W, 20 kHz, Q700 SONICATOR) for 3 h at 30% amplitude. The ultrasound system followed a working cycle of 55 s on and 5 s off. The temperature was maintained at 15 °C by circulating water. Finally, the resultant product was filtered and washed three times with EtOH and water, and then dried overnight in a vacuum oven at 80 °C.

3.2.2. Bi_2O_3 and Bi_2O_3/Cu-MOF

The microwave method was used to synthesize Bi_2O_3 and Cu-MOF/Bi_2O_3. Firstly, 1.2662g $Bi(NO_3)_3{\cdot}5H_2O$ was dissolved in 15 mL of a mixture of EG and EtOH at a volume ratio of 1:3. Then, 0.0064 g of PEG was added to the solution, and the mixture was sonicated for 30 min to achieve complete reaction. Next, the obtained mixture was heated in a microwave reactor (Discover BenchMate system, CEM Co., Tokyo, Japan) with an operating power of 300 W and a temperature of 120 °C for 10 min. Finally, the formed precipitate was collected and washed several times with DI water and EtOH, then dried overnight in a vacuum oven at 80 °C, resulting in the obtained powder of Bi_2O_3. Cu-MOF/Bi_2O_3 was synthesized using the same procedure, with the addition of 0.0064 g of Cu-MOF before the microwave treatment.

3.2.3. Bi_2O_{3-x} and Bi_2O_{3-x}/Cu-MOF

Firstly, 0.2600 g of $NaBH_4$ was added into 200 mL of DMSO and then sonicated for 30 min to completely dissolve it. A quantity of 2 g Bi_2O_3 was added to the mixture and stirring continued for 36 h under aeration N_2 (flow rate of 20 mL/min). Subsequently, the product was collected, washed several times with DI water and EtOH, and then dried overnight in a vacuum oven at 80 °C. The resulting product was denoted Bi_2O_{3-x}. To synthesize Cu-MOF/Bi_2O_{3-x}, the same procedure was followed, but instead of adding Bi_2O_3, 2 g of Cu-MOF/Bi_2O_3 was used.

3.3. Characterizations

The morphologies of the catalysts were observed using a thermal field emission scanning electron microscope (FE-SEM, JEOL JSM-7800F, Tokyo, Japan) and transmission electron microscopy (TEM, JEM2010, JEOL, Tokyo, Japan). X-ray diffraction (XRD) patterns were recorded using a Rigaku Ultima III diffractometer (Tokyo, Japan) with Cu-Kα radiation. The Brunauer–Emmett–Teller (BET) surface area, pore size, and pore volume of the catalysts were measured using the N_2 adsorption method using a Micrometrics ASAP-2020 nitrogen adsorption instrument. UV-visible diffuse reflectance spectra (DRS) were recorded using a Shimadzu UV-2600 spectrophotometer with an integrated sphere attachment, with barium sulfate as the reference. Photoluminescence (PL) properties were measured at room temperature using a Shimadzu RF-3501 spectrometer excited at 400 nm. The particle size distribution was determined using a Shimadzu SALD-2300 through laser diffraction scattering. X-ray photoelectron spectroscopy (XPS) was undertaken using a Physical Electronics PHI 5600 XPS instrument with monochromatic Al-Ka (1486.6 eV) as the excitation source.

3.4. Photocatalytic Activity

A quantity of 0.006 g of photocatalyst was dispersed in 100 mL of a 1,4-D (50 mg/L) solution. Prior to the photocatalytic experiment, the photocatalysts and solution were fully mixed in the dark for 30 min to reach the adsorption equilibrium. The reactor was then illuminated with a 350 W Xenon light (KIT-XENON-ADJ350W, Xenon arc, Bellevue, WA, USA) for 3 h. Samples were collected from the solution at regular intervals and filtered through a 0.22 μm membrane filter before analysis. All experiments were conducted at room temperature, and the solution pH was adjusted using HCl or NaOH. 1,4-D was analyzed using high-performance liquid chromatography (HPLC, LC-10 AT Shimadzu, Kyoto, Japan) equipped with an ultra aquo C18 column (5 μm, 250 mm × 4.6 mm) and a UV detection wavelength of 190 nm. The mobile phase consisted of 95% water and 5% acetonitrile, and the flow rate was set to 1 mL/min. The calibration curve was determined by establishing a linear relationship between known 1,4-D concentrations (0, 10, 20, 30, 40, and 50 mg/L) and HPLC peak areas.

4. Conclusions

In this study, the effects of Cu-MOF and oxygen vacancies on the improvement in the efficiency of 1,4-D degradation by Bi_2O_3 were investigated by preparing Bi_2O_3, Bi_2O_3/Cu-MOF, Bi_2O_{3-x}, and Bi_2O_{3-x}/Cu-MOF. The results showed that Bi_2O_3/Cu-MOF exhibited the highest photocatalytic activity for 1,4-D degradation. This superior performance can be attributed to several factors: the larger specific surface area, well-developed pore structure, and smaller particle size of Bi2O3/Cu-MOF, which provided a considerable number of active sites for catalysis. Meanwhile, the introduction of Cu-MOF enhanced the utilization efficiency of visible light and electron transfer, while the heterojunction promoted the effective separation of photogenerated electron–hole pairs. On the other hand, even though Bi_2O_{3-x} and Bi_2O_{3-x}/Cu-MOF showed excellent optical properties, they surprisingly exhibited lower photocatalytic degradation efficiency of 1,4-D. This can be explained by the crystalline phase transition from β-Bi_2O_3 to α-Bi_2O_3, and the charge compensation effect, which reduced the number of oxidative holes (h^+) induced by oxygen vacancies. Therefore, the utilization of Cu-MOF for constructing heterojunctions significantly enhanced the efficiency of degradation of 1,4-D by Bi_2O_3, while oxygen vacancies and synergism of Cu-MOF and oxygen vacancies have negative effects. Bi_2O_3/Cu-MOF appears a promising photocatalysis for 1,4-D degradation.

Author Contributions: Conceptualization, Q.-Y.W. and J.J.W.; methodology, all authors; formal analysis, W.-M.W. and L.Z.; investigation, W.-M.W.; L.Z. and J.-Y.H.; writing—original draft preparation, W.-M.W.; writing—review editing and supervision, W.-L.W., Q.-Y.W. and J.J.W.; project administration, W.-M.W.; funding acquisition, Q.-Y.W. and J.J.W. All authors have read and agreed to the published version of the manuscript.

Funding: This research was funded by National Science and Technology Council (NSTC), Taiwan (NSTC-111-2221-E-035-017-MY3) and Shenzhen Science, Technology and Innovation Commission, China (Grant No. JCYJ20200109142829123).

Data Availability Statement: Data can be available upon request from the authors.

Acknowledgments: The authors wish to thank for the financial support by the Ministry of Science and Technology (MOST) in Taiwan under the contract numbers of NSTC-111-2221-E-035-017-MY3 and the Shenzhen Science, Technology and Innovation Commission (Grant No. JCYJ20200109142829123).

Conflicts of Interest: The authors declare no conflict of interest.

References

1. Coleman, H.M.; Vimonses, V.; Leslie, G.; Amal, R. Degradation of 1,4-dioxane in water using TiO_2 based photocatalytic and H_2O_2/UV processes. *J. Hazard. Mater.* **2007**, *146*, 496–501. [CrossRef]
2. Qiu, J.; Cheng, J.; Xie, Y.; Jiang, L.; Shi, P.; Li, X.; Swanda, R.V.; Zhou, J.; Wang, Y. 1,4-Dioxane exposure induces kidney damage in mice by perturbing specific renal metabolic pathways: An integrated omics insight into the underlying mechanisms. *Chemosphere* **2019**, *228*, 149–158. [CrossRef] [PubMed]
3. Park, Y.K.; Chung, K.H.; Park, I.S.; Kim, S.C.; Kim, S.J.; Jung, S.C. Photocatalytic degradation of 1,4-dioxane using liquid phase plasma on visible light photocatalysts. *J. Hazard. Mater.* **2020**, *399*, 123087. [CrossRef]
4. Wang, W.; Qiao, Z.; Lee, G.J.; Chen, H.; Ding, L.; Zhu, M.; Liu, N.; Wu, J.J. Preparation of ternary photocatalysts and their application in the degradation of 1,4-dioxane using O_3/UV/photocatalyst process. *Sep. Purif. Technol.* **2020**, *235*, 116194. [CrossRef]
5. Xu, X.; Liu, S.; Sun, P.; Guo, Z.; Smith, K.; Zhang, D.; Li, H.; Bedia, J.; Belver, C. Iron tungstate on nano-γ-alumina as photocatalyst for 1,4-dioxane solar degradation in water. *J. Clean. Prod.* **2022**, *377*, 134232. [CrossRef]
6. Byrne, C.; Rhatigan, S.; Hermosilla, D.; Merayo, N.; Blanco, Á.; Michel, M.C.; Hinder, S.; Nolan, M.; Pillai, S.C. Modification of TiO_2 with hBN: High temperature anatase phase stabilisation and photocatalytic degradation of 1,4-dioxane. *J. Phys. Mater.* **2020**, *3*, 015009. [CrossRef]
7. Ali, N.S.; Kalash, K.R.; Ahmed, A.N.; Albayati, T.M. Performance of a solar photocatalysis reactor as pretreatment for wastewater via UV, UV/TiO_2, and UV/H_2O_2 to control membrane fouling. *Sci. Rep.* **2022**, *12*, 16782. [CrossRef] [PubMed]
8. Liu, G.; Li, S.; Lu, Y.; Zhang, J.; Feng, Z.; Li, C. Controllable synthesis of α-Bi_2O_3 and γ-Bi_2O_3 with high photocatalytic activity by α-$Bi_2O_3 \rightarrow \gamma$-$Bi_2O_3 \rightarrow \alpha$-$Bi_2O_3$ transformation in a facile precipitation method. *J. Alloys Compd.* **2016**, *689*, 787–799. [CrossRef]
9. Han, S.; Li, J.; Yang, K.; Lin, J. Fabrication of a β-Bi_2O_3/BiOI heterojunction and its efficient photocatalysis for organic dye removal. *Chin. J. Catal.* **2015**, *36*, 2119–2126. [CrossRef]
10. Ayekoe, P.Y.; Robert, D.; Goné, D.L. Preparation of effective TiO_2/Bi_2O_3 photocatalysts for water treatment. *Environ. Chem. Lett.* **2016**, *14*, 387–393. [CrossRef]
11. Zhang, J.; Hu, Y.; Jiang, X.; Chen, S.; Meng, S.; Fu, X. Design of a direct Z-scheme photocatalyst: Preparation and characterization of Bi_2O_3/g-C_3N_4 with high visible light activity. *J. Hazard. Mater.* **2014**, *280*, 713–722. [CrossRef] [PubMed]
12. Lu, Y.; Huang, Y.; Zhang, Y.; Cao, J.J.; Li, H.; Bian, C.; Lee, S.C. Oxygen vacancy engineering of $Bi_2O_3/Bi_2O_2CO_3$ heterojunctions: Implications of the interfacial charge transfer, NO adsorption and removal. *Appl. Catal. B Environ.* **2018**, *231*, 357–367. [CrossRef]
13. Ke, J.; Liu, J.; Sun, H.; Zhang, H.; Duan, X.; Liang, P.; Li, X.; Tade, M.O.; Liu, S.; Wang, S. Facile assembly of $Bi_2O_3/Bi_2S_3/MoS_2$ n-p heterojunction with layered n-Bi_2O_3 and p-MoS_2 for enhanced photocatalytic water oxidation and pollutant degradation. *Appl. Catal. B Environ.* **2017**, *200*, 47–55. [CrossRef]
14. Liu, J.; Ma, N.; Wu, W.; He, Q. Recent progress on photocatalytic heterostructures with full solar spectral responses. *Chem. Eng. J.* **2020**, *393*, 124719. [CrossRef]
15. Furukawa, H.; Cordova, K.E.; O'Keeffe, M.; Yaghi, O.M. The chemistry and applications of metal-organic frameworks, (1095-9203 (Electronic)). *Science* **2013**, *341*, 1230444. [CrossRef]
16. Akbarzadeh, E.; Soheili, H.Z.; Hosseinifard, M.; Gholami, M.R. Preparation and characterization of novel Ag_3VO_4/Cu-MOF/rGO heterojunction for photocatalytic degradation of organic pollutants. *Mater. Res. Bull.* **2020**, *121*, 110621. [CrossRef]
17. Zhao, K.; Zhang, Z.; Feng, Y.; Lin, S.; Li, H.; Gao, X. Surface oxygen vacancy modified Bi_2MoO_6/MIL-88B(Fe) heterostructure with enhanced spatial charge separation at the bulk & interface. *Appl. Catal. B Environ.* **2020**, *268*, 118740.
18. Ding, R.R.; Li, W.Q.; He, C.S.; Wang, Y.R.; Liu, X.C.; Zhou, G.N.; Mu, Y. Oxygen vacancy on hollow sphere $CuFe_2O_4$ as an efficient Fenton-like catalysis for organic pollutant degradation over a wide pH range. *Appl. Catal. B Environ.* **2021**, *291*, 120069. [CrossRef]
19. Zou, X.; Mei, Z.; Jiang, J.; Guo, H. MOFs-derived Bi_2O_3@C with rich oxygen vacancies through rapid thermal annealing technology for photodegradation of tetracycline hydrochloride. *Appl. Surf. Sci.* **2022**, *586*, 152813. [CrossRef]

20. Lin, K.S.; Adhikari, A.K.; Ku, C.-N.; Chiang, C.-L.; Kuo, H. Synthesis and characterization of porous HKUST-1 metal organic frameworks for hydrogen storage. *Int. J. Hydrogen Energy* **2012**, *37*, 13865–13871. [CrossRef]
21. Di, J.; Xia, J.; Ji, M.; Wang, B.; Yin, S.; Xu, H.; Chen, Z.; Li, H. Carbon Quantum Dots Induced Ultrasmall BiOI Nanosheets with Assembled Hollow Structures for Broad Spectrum Photocatalytic Activity and Mechanism Insight. *Langmuir* **2016**, *32*, 2075–2084. [CrossRef] [PubMed]
22. da Silva, G.G.; Machado, F.L.A.; Junior, S.A.; Padrón-Hernández, E. Metal-organic framework: Structure and magnetic properties of $[Cu_3(BTC)_2\ (L)_x{\cdot}(CuO)_y]_n$ (L=H_2O, DMF). *J. Solid State Chem.* **2017**, *253*, 1–5.
23. Kumaraguru, S.; Nivetha, R.; Gopinath, K.; Sundaravadivel, E.; Almutairi, B.O.; Almutairi, M.H.; Mahboob, S.; Kavipriya, M.R.; Nicoletti, M.; Govindarajan, M. Synthesis of Cu-MOF/CeO_2 nanocomposite and their evaluation of hydrogen production and cytotoxic activity. *J. Mater. Res. Technol.* **2022**, *18*, 1732–1745. [CrossRef]
24. Lee, G.J.; Chien, Y.W.; Anandan, S.; Lv, C.; Dong, J.; Wu, J.J. Fabrication of metal-doped BiOI/MOF composite photocatalysts with enhanced photocatalytic performance. *Int. J. Hydrogen Energy* **2021**, *46*, 5949–5962. [CrossRef]
25. Fan, M.; Wang, W.D.; Zhu, Y.; Sun, X.; Zhang, F.; Dong, Z. Palladium clusters confined in triazinyl-functionalized COFs with enhanced catalytic activity. *Appl. Catal. B Environ.* **2019**, *257*, 117942. [CrossRef]
26. Hwang, H.; Shin, J.-H.; Lee, K.Y.; Choi, W. Facile one-pot transformation using structure-guided combustion waves of micro-nanostructured β-Bi_2O_3 to α-Bi_2O_3@C and analysis of electrochemical capacitance. *Appl. Surf. Sci.* **2018**, *428*, 422–431. [CrossRef]
27. Bilecka, I.; Niederberger, M. Microwave chemistry for inorganic nanomaterials synthesis. *Nanoscale* **2010**, *2*, 1358–1374. [CrossRef]
28. Huang, Q.; Zhang, S.; Cai, C.; Zhou, B. β- and α-Bi_2O_3 nanoparticles synthesized via microwave-assisted method and their photocatalytic activity towards the degradation of rhodamine B. *Mater. Lett.* **2011**, *65*, 988–990. [CrossRef]
29. Zhou, H.; Wen, Z.; Liu, J.; Ke, J.; Duan, X.; Wang, S. Z-scheme plasmonic Ag decorated WO_3/Bi_2WO_6 hybrids for enhanced photocatalytic abatement of chlorinated-VOCs under solar light irradiation. *Appl. Catal. B Environ.* **2019**, *242*, 76–84. [CrossRef]
30. He, W.; Wei, Y.; Xiong, J.; Tang, Z.; Wang, Y.; Wang, X.; Deng, J.; Yu, X.; Zhang, X.; Zhao, Z. Boosting Selective Photocatalytic CO_2 Reduction to CO over Dual-core@shell Structured Bi_2O_3/Bi_2WO_6@g-C_3N_4 Catalysts with Strong Interaction Interface. *Sep. Purif. Technol.* **2022**, *300*, 121850. [CrossRef]
31. Kan, L.; Mu, W.; Chang, C.; Lian, F. Dual S-scheme graphitic carbon-doped α-Bi_2O_3/β-Bi_2O_3/Bi_5O_7I ternary heterojunction photocatalyst for the degradation of Bisphenol A. *Sep. Purif. Technol.* **2023**, *312*, 123388. [CrossRef]
32. Chen, J.; Zhong, J.; Li, J.; Qiu, K. Boosted photocatalytic removal of tetracycline on S-scheme $Bi_{12}O_{17}C_{12}$/α-Bi_2O_3 heterojunctions with rich oxygen vacancies. *Appl. Surf. Sci.* **2021**, *563*, 150246. [CrossRef]
33. Jiang, H.; Xu, M.; Zhao, X.; Wang, H.; Huo, P. Fabricated local surface plasmon resonance Cu_2O/Ni-MOF hierarchical heterostructure photocatalysts for enhanced photoreduction of CO_2. *J. Environ. Chem. Eng.* **2023**, *11*, 109504. [CrossRef]
34. Qiao, Z.; Wang, W.; Liu, N.; Huang, H.T.; Karuppasamy, L.; Yang, H.J.; Liu, C.H.; Wu, J.J. Synthesis of MOF/MoS_2 composite photocatalysts with enhanced photocatalytic performance for hydrogen evolution from water splitting. *Int. J. Hydrogen Energy* **2022**, *47*, 40755–40767. [CrossRef]
35. Tonda, S.; Kumar, S.; Bhardwaj, M.; Yadav, P.; Ogale, S. g-C_3N_4/NiAl-LDH 2D/2D Hybrid Heterojunction for High-Performance Photocatalytic Reduction of CO_2 into Renewable Fuels. *ACS Appl. Mater. Interfaces* **2018**, *10*, 2667–2678. [CrossRef] [PubMed]
36. Ye, M.; Wu, X.; Li, C.; Song, B.; Ma, X.; Liu, S.J.A.S.S. Insights into Boosting Photoelectrochemical Performance Over $Cu_3(BTC)_2$ Passivated Cu_2O Nanorod Arrays. *Adv. Sustain. Syst.* **2022**, *6*, 2200272. [CrossRef]
37. Wang, W.M.; Tseng, S.J.; Huang, Y.S.; Wu, Q.Y.; Wang, W.L.; Wu, J.J. Hollow-structured Pd/TiO2 as a dual functional photocatalyst for methyl orange oxidation and selective reduction of nitrate into nitrogen. *J. Ind. Eng. Chem.* **2023**, *119*, 386–394. [CrossRef]
38. Wang, W.; Li, B.; Yang, H.J.; Liu, Y.; Gurusamy, L.; Karuppasamy, L.; Wu, J.J. Photocatalytic Hydrogen Evolution from Water Splitting Using Core-Shell Structured Cu/ZnS/COF Composites. *Nanomaterials* **2021**, *11*, 3380. [CrossRef]
39. Wang, M.; Chen, J.; Hu, L.; Wei, Y.; Xu, Y.; Wang, C.; Gao, P.; Liu, Y.; Liu, C.; Song, Y.; et al. Heterogeneous interfacial photocatalysis for the inactivation of Karenia mikimotoi by Bi_2O_3 loaded onto a copper metal organic framework (Bi_2O_3@Cu-MOF) under visible light. *Chem. Eng. J.* **2023**, *456*, 141154. [CrossRef]
40. Ren, Y.; Zeng, D.; Ong, W.-J. Interfacial engineering of graphitic carbon nitride (g-C_3N_4)-based metal sulfide heterojunction photocatalysts for energy conversion: A review. *Chin. J. Catal.* **2019**, *40*, 289–319. [CrossRef]
41. Xu, X.; Liu, S.; Cui, Y.; Wang, X.; Smith, K.; Wang, Y. Solar-Driven Removal of 1,4-Dioxane Using WO_3/nγ-Al_2O_3 Nano-catalyst in Water. *Catalysts* **2019**, *9*, 389. [CrossRef]
42. Youn, N.K.; Heo, J.E.; Joo, O.S.; Lee, H.; Kim, J.; Min, B.K. The effect of dissolved oxygen on the 1,4-dioxane degradation with TiO_2 and Au–TiO_2 photocatalysts. *J. Hazard. Mater.* **2010**, *177*, 216–221. [CrossRef] [PubMed]
43. Min, B.K.; Heo, J.E.; Youn, N.K.; Joo, O.S.; Lee, H.; Kim, J.H.; Kim, H.S. Tuning of the photocatalytic 1,4-dioxane degradation with surface plasmon resonance of gold nanoparticles on titania. *Catal. Commun.* **2009**, *10*, 712–715. [CrossRef]
44. Samy, M.; Alalm, M.G.; Khalil, M.N.; Ezeldean, E.; El-Dissouky, A.; Nasr, M.; Tawfik, A. Treatment of hazardous landfill leachate containing 1,4 dioxane by biochar-based photocatalysts in a solar photo-oxidation reactor. *J. Environ. Manag.* **2023**, *332*, 117402. [CrossRef]
45. Lu, Y.; Zhao, Y.; Zhao, J.; Song, Y.; Huang, Z.; Gao, F.; Li, N.; Li, Y. Induced Aqueous Synthesis of Metastable β-Bi_2O_3 Microcrystals for Visible-Light Photocatalyst Study. *Cryst. Growth Des.* **2015**, *15*, 1031–1042. [CrossRef]
46. Wang, D.; Zhu, R.; Lou, J.; Yuan, J.; Xu, J.; Fan, X. Novel marigold-like CuO@Cu-based MOFs composite photocatalyst for high-performance removal of alkylphenol ethoxylate under visible light. *J. Environ. Chem. Eng.* **2021**, *9*, 106434. [CrossRef]

47. Pirhashemi, M.; Elhag, S.A.O.; Adam, R.A.O.X.; Habibi-Yangjeh, A.; Liu, X.; Willander, M.; Nur, O.A.O.X. n-n ZnO-Ag_2CrO_4 heterojunction photoelectrodes with enhanced visible-light photoelectrochemical properties. *RSC Adv.* **2019**, *9*, 7992. [CrossRef]
48. Ghosh, S.; Bera, S.; Singh, A.; Basu, S.; Basu, R.N. Hierarchical Bi_2WO_6/$BiFeWO_6$ n-n heterojunction as an efficient photocatalyst for water splitting under visible light. *J. Alloys Compd.* **2022**, *919*, 165700. [CrossRef]
49. Pirhashemi, M.; Habibi-Yangjeh, A. Novel ZnO/Ag_2CrO_4 nanocomposites with n–n heterojunctions as excellent photocatalysts for degradation of different pollutants under visible light. *J. Mater. Sci. Mater. Electron.* **2016**, *27*, 4098–4108. [CrossRef]
50. Gao, C.; Liu, G.; Liu, X.; Wang, X.; Liu, M.; Chen, Y.; Jiang, X.; Wang, G.; Teng, Z.; Yang, W. Flower-like n-Bi_2O_3/n-BiOCl heterojunction with excellent photocatalytic performance for visible light degradation of Bisphenol A and Methylene blue. *J. Alloys Compd.* **2022**, *929*, 167296. [CrossRef]